

## MULTIBODY ANALYSIS OF A MICRO-AERIAL VEHICLE FLAPPING WING

Pierangelo Masarati\*, Marco Morandini\*, Giuseppe Quaranta\* and Riccardo Vescovini\*

\*Dipartimento di Ingegneria Aerospaziale  
Politecnico di Milano, via La Masa 34, 20156, Milano — Italy  
e-mails: pierangelo.masarati@polimi.it, marco.morandini@polimi.it,  
giuseppe.quaranta@polimi.it, riccardo.vescovini@mail.polimi.it  
web page: <http://www.aero.polimi.it/>

**Keywords:** Shell, Micro aerial vehicles, Flapping wing, Fluid structure interaction.

**Abstract.** *This paper discusses the use of multibody dynamics, augmented by the direct implementation of nonlinear finite element beams and significantly shells, to perform the coupled structural and fluid-dynamics analysis of flapping wing Micro-Aerial Vehicles. The implementation of the shell formulation in a free general-purpose multibody solver is described and validated. The solver, coupled to a free-wake aerodynamic model based on vortex-lattice, is applied to the analysis of a very flexible MAV flapping wing. Encouraging results have been obtained, which illustrate how the structural model should be able to capture the physics of the problem when coupled with more sophisticated aerodynamic models.*

## 1 INTRODUCTION

Micro-Aerial Vehicles (MAV) capable of hovering and forward flight represent an interesting means to provide reconnaissance and surveillance capabilities in dangerous environments, for both military and civil tasks. Foreseen applications consist in inspecting dangerous environments, including urban battlefields, caves, mines, and hazardous places like chemical plants during emergency operations.

The problem presents many issues from the analysis point of view. The aerodynamic flow field is characterized by very low Mach and Reynolds numbers; however, the problem appears to be dominated by the significant unsteadiness of the flow rather than by viscosity itself, with separations occurring at both the trailing and the leading edge of the wings. The resulting vortical structures remain in the vicinity of the wing, especially in hover or at very low speed.

The problem has been analyzed from different points of view: aerodynamics [1–6], aeroelasticity [7, 8], kinematics and structural dynamics [9–12], systemics [13, 14], testing [15, 16].

The capability to analyze the problem is important because direct prototyping, although not extremely expensive, can be significantly time consuming and error prone. The problem requires the capability to address structural dynamics with significant geometrical nonlinearity, mechanism modeling capability to take into account the actual flapping and pitch mechanism, and consistent fluid-structure coupling. Multibody System Dynamics (MSD) represents an ideal modeling environment to address this type of problems, since it allows to directly consider sophisticated structural dynamics and mechanism modeling. At the same time, the analysis can be consistently coupled to external solvers for the Computational Fluid Dynamics (CFD) part of the problem. The free general-purpose multibody solver MBDyn is used as the core of the coupled simulation.

Membrane-based insect-like MAV have been proposed for example in [17]. This work presents the implementation of a consistent geometrically nonlinear four-node shell element that is used, in conjunction to an already available nonlinear beam element [18], to model a flapping wing model manufactured and tested by Malhan *et al.* [16] within the MAST/CTA project sponsored by the US Army. A consistent meshless approach is used to model Fluid-Structure Interaction (FSI). It is based on Moving Least Squares (MLS) using Radial Basis Functions (RBF) and represents a very efficient and reliable way to couple a multifield analysis with possibly incompatible interface boundaries. In this work free wake analysis, modeled using a vortex-lattice formulation, is coupled to the detailed structural analysis. The essentially inviscid fluid dynamics model is not expected to give an accurate prediction of airloads. However, it is considered sufficient to validate the soundness of the structural model, in view of its subsequent coupling with more sophisticated CFD analysis.

The use of shell elements either in Finite Element (FE) or in MSD analysis to model flapping wing MAV has been recently proposed, for example, by Chandar and Damodaran [19] and Chimakurthi *et al.* [20]. The novelty of the approach used in this work is related to the use of a truly nonlinear shell model, as opposed to the co-rotational one of [20], and to the use of a consistent mapping of the interaction between the structural and the CFD analysis.

## 2 STRUCTURAL MODEL

A four node  $C^0$  shell element has been implemented to allow the modeling of arbitrary 2-D structural elements. It is derived from the elements proposed by Witkowski [21], based on a combination of the Enhanced Assumed Strain (EAS) and Assumed Natural Strain (ANS) formulations.

## 2.1 4-Node Shell Element Formulation

Let  $\mathbf{y}$  be the position of the shell reference surface, and define a local orthogonal coordinate system on the undeformed shell surface. Let  $\mathbf{T}$  also be a local orthonormal triad defined on the surface. Two Biot-like linear deformation vectors can be computed by comparing the deformed and undeformed back-rotated derivatives of the position, i.e.

$$\tilde{\boldsymbol{\epsilon}}_k = \mathbf{T}^T \mathbf{y}_{/k} - \mathbf{T}_0^T \mathbf{y}_{0/k} \quad (1)$$

where  $\mathbf{y}_{/k}$  is the partial derivative with respect to the arc length coordinate  $k$  ( $k = 1, 2$ ); the subscript  $(\cdot)_0$  identifies the undeformed configuration. Vectors  $\tilde{\boldsymbol{\epsilon}}_k$  are work-conjugated with the force per unit length vectors  $\mathbf{n}_k$ . The Biot-like angular deformation is defined as

$$\tilde{\mathbf{k}}_k = \mathbf{T}^T \mathbf{k}_k - \mathbf{T}_0^T \mathbf{k}_{0k}, \quad (2)$$

where  $\mathbf{k}_k$  is the vector characterizing the spatial derivative of tensor  $\mathbf{T}$ , with respect to arc length coordinate  $k$ , i.e.

$$\mathbf{k}_k \times = \mathbf{T}_{/k} \mathbf{T}^T. \quad (3)$$

The angular strain vectors are work-conjugated with the internal couple per unit length vectors  $\mathbf{m}_k$ . The straining of the shell is thus completely defined by the vector

$$\boldsymbol{\epsilon} = \begin{Bmatrix} \tilde{\boldsymbol{\epsilon}}_1 \\ \tilde{\boldsymbol{\epsilon}}_2 \\ \tilde{\mathbf{k}}_1 \\ \tilde{\mathbf{k}}_2 \end{Bmatrix}, \quad (4)$$

which is work-conjugated to

$$\boldsymbol{\sigma} = \begin{Bmatrix} \mathbf{n}_1 \\ \mathbf{n}_2 \\ \mathbf{m}_1 \\ \mathbf{m}_2 \end{Bmatrix}. \quad (5)$$

The virtual internal work is thus equal to

$$\delta L_i = \int_A \delta \boldsymbol{\epsilon}^T \boldsymbol{\sigma} dA \quad (6)$$

The proposed formulation departs from Witkowski's one [21] and from the earlier work of Chróścielewski and Witkowski [22] in the treatment of the rotation field. The orientation field  $\mathbf{T}$  is interpolated resorting to a co-rotational framework, just like in the above cited works. In this work, however, the angular strain vectors  $\tilde{\mathbf{k}}_k$  are computed from their definition Eq. (2), and not from the back-rotated gradient of the rotation tensor  $\tilde{\boldsymbol{\Phi}} = \mathbf{T} \mathbf{T}_0^T$ . Furthermore, the direct use of Eqs. (1, 2) and of their work-conjugated forces per unit length nullifies the need to resort to co-rotational derivatives in the definition of the strain vectors. The linearization of the ensuing virtual internal work differs as well, as the above cited works seems to miss a term related to the second variation of the angular strain vectors  $\partial \delta \tilde{\mathbf{k}}_k$ .

The interpolation of the orientation field is performed after defining in the reference configuration a triad of unit orthogonal vectors  $\mathbf{t}_{n1}, \mathbf{t}_{n2}, \mathbf{t}_{n3}$  for each node  $n$ , with  $\mathbf{t}_{n1}$  and  $\mathbf{t}_{n2}$  tangent to the shell surface and  $\mathbf{t}_{n3} = \mathbf{t}_{n1} \times \mathbf{t}_{n2}$ . Let  $\mathbf{R}_n$  be the orientation tensor of the node, and define the local shell orientation as

$$\mathbf{T}_n = \mathbf{R}_n \mathbf{R}_{0n}^T [\mathbf{t}_{n1}, \mathbf{t}_{n2}, \mathbf{t}_{n3}], \quad (7)$$

where  $\mathbf{R}_{0n}$  is the nodal orientation in the reference configuration. The average orientation  $\bar{\mathbf{T}}$  of the shell is then computed as  $\bar{\mathbf{T}} = \exp(\log(1/N \sum_{n=1,N} \mathbf{T}_n))$ , where  $N$  is the number of nodes,  $\log()$  extracts a skew symmetric tensor, say  $\mathbf{a} \times$ , and  $\exp(\mathbf{a} \times)$  computes the rotation tensor defined by the rotation vector  $\mathbf{a}$ . Standard bilinear interpolation shape functions  $N_n(\xi)$  are then defined for each node  $n$  and used to interpolate the relative rotation vectors that define the relative nodal rotations  $\tilde{\mathbf{R}}_n = \bar{\mathbf{T}}^T \mathbf{T}_n$ , i.e.  $\tilde{\varphi}(\xi) \times = \log(\tilde{\mathbf{R}}) = \sum_{n=1,N} N_n(\xi) \log(\bar{\mathbf{T}}^T \mathbf{T}_n)$ ; the interpolated orientation can finally be recovered as  $\mathbf{T}_i = \bar{\mathbf{T}} \exp(\tilde{\varphi}_i \times)$ . Computing the virtual internal work Eq. (6) and its linearization involves computing the first ( $\delta$ ) and second ( $\partial\delta$ ) variations of the linear and angular deformation vectors Eqs. (1, 2). These, in turn, require explicit expressions for the interpolated virtual rotation vector  $\varphi_{i\delta}$ , defined by  $\varphi_{i\delta} \times = \delta \mathbf{T}_i \mathbf{T}_i^T$ ; recall that the virtual rotation vector  $\varphi_\delta$  can be computed from the virtual variation of the rotation vector as  $\varphi_\delta = \Gamma(\varphi) \delta \varphi$ , with  $\Gamma(\varphi)$  a second order tensor. The interpolated virtual rotation vector is

$$\varphi_{i\delta} = \sum_{n=1,N} \Phi_{in} N_{in} \varphi_{n\delta} \quad (8)$$

with

$$\Phi_{in} = \bar{\mathbf{T}} \tilde{\Gamma}_i \tilde{\Gamma}_n^{-1} \bar{\mathbf{T}}^T. \quad (9)$$

The first variation of the linear strain is then

$$\delta(\mathbf{T}_i^T \mathbf{y}_{i/k}) = \mathbf{T}_i^T (\mathbf{y}_{i/k} \times \varphi_{i\delta} + \delta \mathbf{y}_{i/k}), \quad (10)$$

with the second variation equal to

$$\partial\delta(\mathbf{T}_i^T \mathbf{y}_{i/k}) = \mathbf{T}_i^T ((\mathbf{y}_{i/k} \times \varphi_{i\delta} + \delta \mathbf{y}_{i/k}) \times \varphi_{i\partial} - \varphi_{i\delta} \times \partial \mathbf{y}_{i/k} + \mathbf{y}_{i/k} \times \partial \varphi_{i\delta}). \quad (11)$$

The back-rotated curvature follows

$$\mathbf{T}_i^T \mathbf{k}_{ik} = \tilde{\Gamma}_i^T \sum_{n=1,N} N_{in/k} \tilde{\varphi}_n, \quad (12)$$

with its first

$$\begin{aligned} \delta(\mathbf{T}_i^T \mathbf{k}_{ik}) &= \mathbf{T}_i^T \mathbf{k}_{ik} \times \varphi_{i\delta} + \mathbf{T}_i^T \delta \mathbf{k}_{ik} \\ \text{FIXME: check} &= \mathbf{T}_i^T \varphi_{i\delta/k} \\ \text{FIXME: check} &= \mathbf{T}_i^T \sum_{n=1,N} (\Phi_{in/k} N_{in} + \Phi_{in} N_{in/k}) \varphi_{n\delta} \end{aligned} \quad (13)$$

(thanks to the fact that according to Schwartz's theorem  $\delta(\mathbf{T}_{i/k}) = (\delta \mathbf{T}_i)_{/k}$ ) and second variation

$$\partial\delta(\mathbf{T}_i^T \mathbf{k}_{ik}) = \partial(\mathbf{T}_i^T \mathbf{k}_{ik} \times \varphi_{i\delta} + \mathbf{T}_i^T \delta \mathbf{k}_{ik}) \quad (14a)$$

$$= -\mathbf{T}_i^T \varphi_{i\partial} \times \mathbf{k}_{ik} \times \varphi_{i\delta} + \mathbf{T}_i^T \partial \mathbf{k}_{ik} \times \varphi_{i\delta} + \mathbf{T}_i^T \partial \delta \mathbf{k}_{ik} \quad (14b)$$

$$\text{FIXME: check} = \partial(\mathbf{T}_i^T \varphi_{i\delta/k}) = \mathbf{T}_i^T (\varphi_{i\delta/k} \times \varphi_{i\partial} + \partial \varphi_{i\delta/k}) \quad (14c)$$

$$\begin{aligned} \text{FIXME: check} &= \mathbf{T}_i^T \left( \left( \sum_{n=1,N} (\Phi_{in/k} N_{in} + \Phi_{in} N_{in/k}) \varphi_{n\delta} \right) \times \sum_{n=1,N} \Phi_{in} N_{in} \varphi_{n\partial} \right. \\ &\quad \left. + \sum_{n=1,N} (\partial \Phi_{in/k} N_{in} + \partial \Phi_{in} N_{in/k}) \varphi_{n\delta} \text{FIXME?} \right). \end{aligned} \quad (14d)$$

It is worth noticing that the last term of Eq. (14b), whose explicit expression turns out to be rather complex, seems to be missing from Chróścielewski and Witkowski's works. Explicit formulæ for the derivatives of the rotation tensor up to the third order, required in order to consistently linearize the approximated deformation field, can be found in Merlini and Morandini [23].

## 2.2 Constitutive Properties

The constitutive law of the shell must be computed beforehand; it relates the generalized stress vector Eq. (5) as a function of the generalized deformation vector Eq. (4). As an example, the constitutive law of an isotropic flat plate is

$$\begin{Bmatrix} \mathbf{n}_1 \\ \mathbf{n}_2 \\ \mathbf{m}_1 \\ \mathbf{m}_2 \end{Bmatrix} = \mathbb{D} \begin{Bmatrix} \tilde{\epsilon}_1 \\ \tilde{\epsilon}_2 \\ \tilde{\mathbf{k}}_1 \\ \tilde{\mathbf{k}}_2 \end{Bmatrix} \quad (15)$$

with

$$\mathbb{D} = \begin{bmatrix} C & 0 & 0 & 0 & C\nu & 0 & 0 & 0 & 0 & 0 & 0 & 0 \\ 0 & 2Gh & 0 & 0 & 0 & 0 & 0 & 0 & 0 & 0 & 0 & 0 \\ 0 & 0 & \alpha Gh & 0 & 0 & 0 & 0 & 0 & 0 & 0 & 0 & 0 \\ 0 & 0 & 0 & 2Gh & 0 & 0 & 0 & 0 & 0 & 0 & 0 & 0 \\ C\nu & 0 & 0 & 0 & C & 0 & 0 & 0 & 0 & 0 & 0 & 0 \\ 0 & 0 & 0 & 0 & 0 & \alpha Gh & 0 & 0 & 0 & 0 & 0 & 0 \\ 0 & 0 & 0 & 0 & 0 & 0 & 2F & 0 & 0 & 0 & 0 & 0 \\ 0 & 0 & 0 & 0 & 0 & 0 & 0 & D & 0 & -D\nu & 0 & 0 \\ 0 & 0 & 0 & 0 & 0 & 0 & 0 & 0 & \beta F & 0 & 0 & 0 \\ 0 & 0 & 0 & 0 & 0 & 0 & 0 & -D\nu & 0 & D & 0 & 0 \\ 0 & 0 & 0 & 0 & 0 & 0 & 0 & 0 & 0 & 0 & 2F & 0 \\ 0 & 0 & 0 & 0 & 0 & 0 & 0 & 0 & 0 & 0 & 0 & \beta F \end{bmatrix}, \quad (16)$$

$C = E/(1 - \nu^2)h$ ,  $D = Ch^2/12$ ,  $F = Gh^3/12$ ,  $E$  Young's modulus,  $\nu$  Poisson's coefficient,  $G = E/(2(1 + \nu))$  the shear modulus, and  $h$  the shell thickness; the coefficients  $\alpha$  and  $\beta$  are the shear and moment factors. The constitutive law for laminated plates can be easily estimated using the Classical Lamination Theory (CLT), but is better computed using appropriate formulations, as the one described in Masarati and Ghiringhelli [24], which take into account the effects of natural and kinematic inter-laminar boundary conditions on the stiffness of the shell.

## 2.3 Static Analysis Verification

The soundness of the proposed implementation is illustrated by the capability to comply, within the desired accuracy, with well-known static benchmarks that require the shell model to undergo significantly large deformations.

### 2.3.1 Cantilever subjected to end shear force

This test case is illustrated in Section 3.1 of [25]. It consists of a cantilever subjected to a shear force at the free end directed along the thickness when undeformed. The direction of the force remains constant while the load increases to the limit value. Figure 1(b) compares the

components of the tip node displacement for the  $16 \times 1$  mesh with those reported in [25]. The  $8 \times 1$  mesh essentially yields the same result.

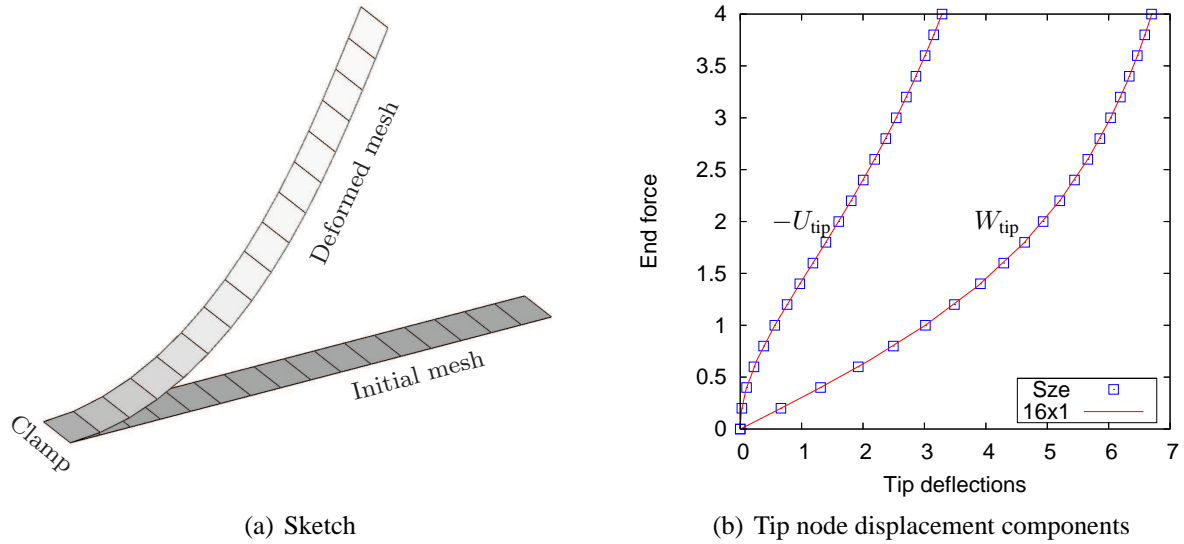


Figure 1: Cantilever subjected to end shear force (Example 3.1 from [25])

### 2.3.2 Slit annular plate subjected to lifting line force

Example 3.3 of [25], illustrated in Fig. 2(a), consists in a vertical axis slit annular plate, clamped at one side of the slit and subjected to a vertical line force. Figure 2(b) compares the vertical displacement of the two end points of the free slit side for the  $10 \times 80$  mesh with those reported in [25]. The much coarser  $6 \times 30$  mesh yields slightly different results.

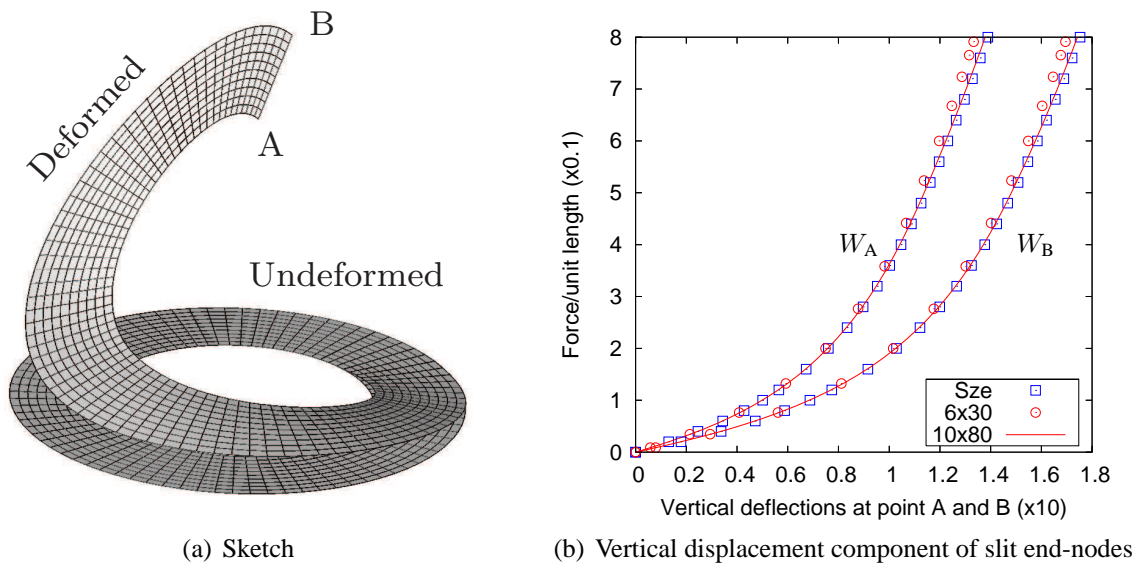


Figure 2: Slit annular plate subjected to lifting line force (Example 3.3 from [25])

### 2.3.3 Pullout of an open-ended cylindrical shell

Example 3.5 of [25], illustrated in Fig. 3(a), consists in an open-ended cylindrical shell subjected to pullout forces at two points along a diameter at mid-height. Thanks to symmetry, only one-eighth of the problem is modeled. Figure 3(b) compares three noteworthy displacement components for the  $16 \times 14$  and  $24 \times 36$  meshes with those reported in [25]. The two meshes yield nearly identical results.

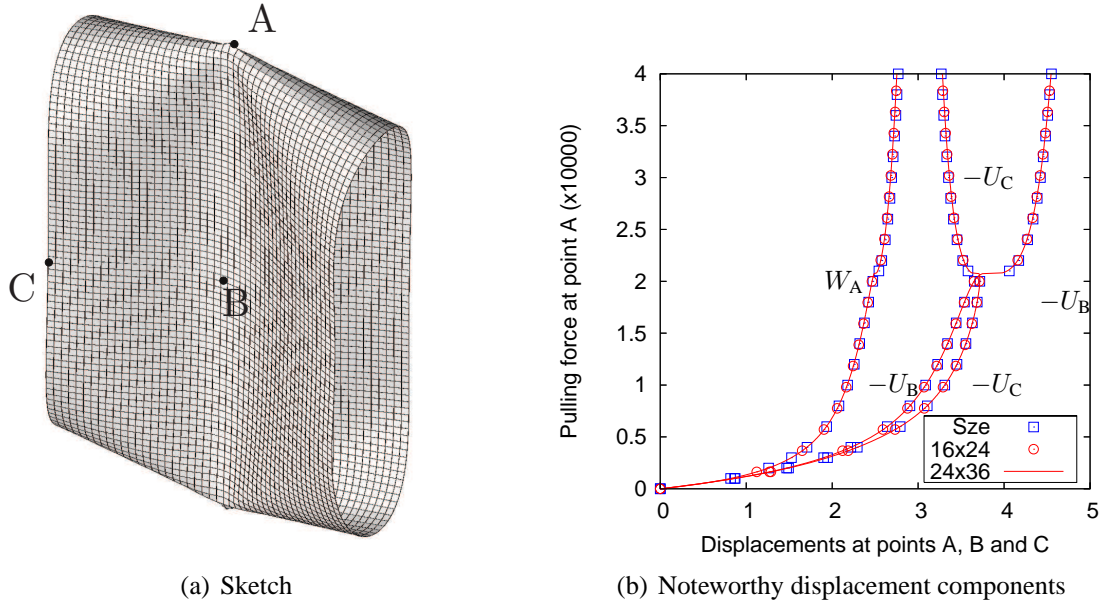


Figure 3: Pullout of an open-ended cylindrical shell (Example 3.5 from [25])

### 2.3.4 Pinched cylindrical shell mounted over rigid diaphragms

Example 3.6 of [25], illustrated in Fig. 4(a), consists in a cylindrical shell with end diaphragms that prevent radial displacement subjected to radial compression forces at two points along a diameter at mid-height. Thanks to symmetry, only one-eighth of the problem is modeled. Figure 4(b) compares two noteworthy displacement components for the  $40 \times 40$  and  $48 \times 48$  meshes with those reported in [25] for the isotropic material case. The two meshes yield nearly identical results as soon as the analysis converged, namely shortly after a snap-through. Figure 4(c) plots the same data when the displacement of the loaded point is imposed.

## 2.4 Dynamic Analysis Verification

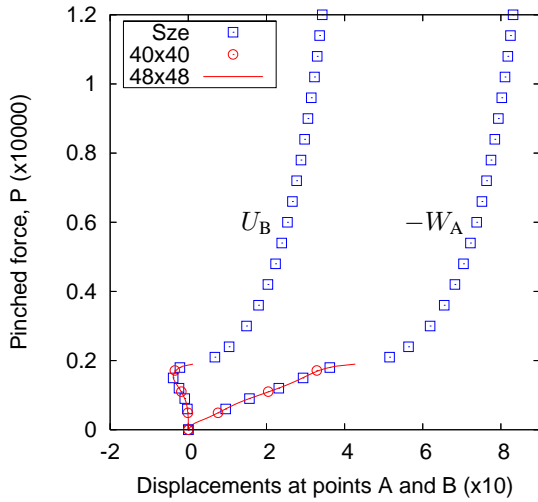
### 2.4.1 Eigenanalysis of cantilever

The problem of Section 2.3.1 (3.1 of [25]) is modified by considering its dynamics when the uniform density of the cantilever is set to  $\rho = 3.13142 \times 10^{-4}$  to set the first bending frequency to 10 Hz, according to

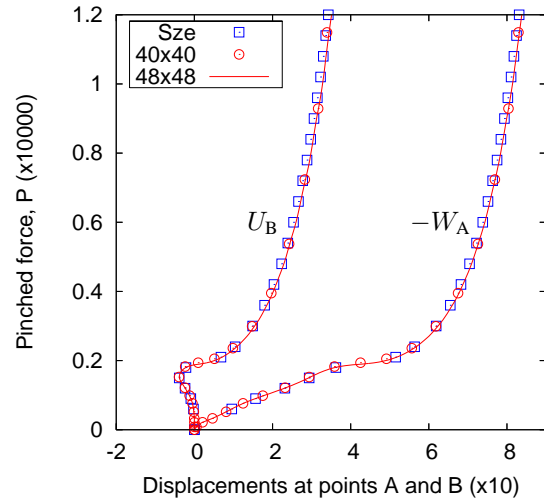
$$\rho = \left( \frac{k}{L} \right)^4 \frac{EJ}{\omega_0^2 A}, \quad (17)$$



(a) Sketch



(b) Noteworthy displacement components



(c) Same as Figure 4(b), imposed displacement

Figure 4: Pinched cylindrical shell mounted over rigid diaphragms (Example 3.6 from [25])

with  $k \cong 1.8751$ .

The inertia of the problem is modeled using rigid bodies lumped at each node, with the center of mass appropriately offset. The transient resulting from a transverse perturbation of the system is analyzed using the Proper Orthogonal Decomposition (POD) as illustrated in [26]. This allows to assess the correctness of the residual in the multibody implementation of the shell element.

The analysis, with a time step of 0.001 s corresponding to 100 steps per period to guarantee accurate integration, yields 10.0315 Hz for the first bending frequency. The direct eigenanalysis is subsequently performed using the procedure illustrated in [27]. This allows to assess the correctness of the linearization of the problem; it yields 10.0355 Hz. The two results are fairly consistent; the error in both cases is about 0.3%.

### 2.4.2 Cantilevered rectangular plate in single degree-of-freedom flap rotation

This example is presented as Case 4 in [20]. It consists in a rectangular beam-like model of 80 mm span, 27 mm chord, and 0.2 mm thickness ( [20] erroneously reports 2 mm), made of Aluminum alloy with Young’s modulus 70 GPa, Poisson’s modulus 0.3, and density 2700 kg/m<sup>3</sup>, clamped at one corner on a 5 by 5 mm square. Flapping is enforced about an axis directed along the root chord, by prescribing the motion of the clamped portion as a flap oscillation about the chordwise root axis according to the function  $\beta(t) = A(1 - \cos(2\pi ft))$ , with  $A = 17$  deg and  $f = 5$  and 30 Hz. The model consists of a 32×9 shells mesh, consisting of 288 elements and 330 nodes; in [20], 512 three-node elements were used, so the mesh refinement is comparable. The vertical component of the displacement of the tip node, normalized with respect to the span, is compared with results presented in [20] in Fig. 5.

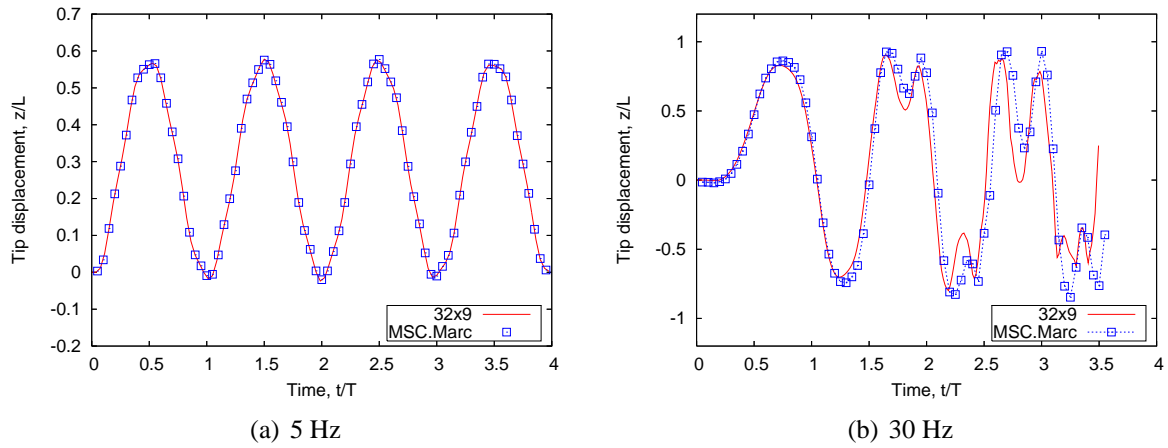


Figure 5: Cantilevered rectangular plate in single degree-of-freedom flap rotation (Case 4 from [20])

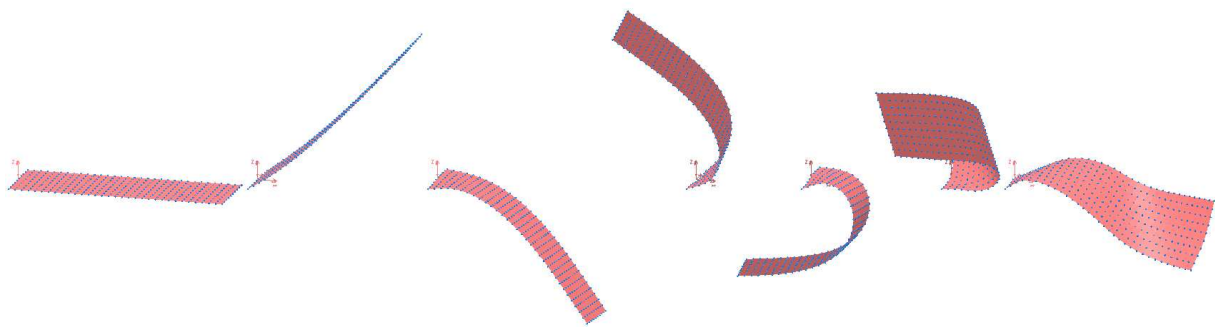


Figure 6: Cantilevered rectangular plate in single degree-of-freedom flap rotation (Case 4 from [20]): sketch of motion with 30 Hz excitation.

The results obtained with the co-rotational shell formulation proposed in that work, called UM/NLAMs, were originally compared with similar results obtained using the commercial solver MSC.Marc. Figure 5(a) refers to a 5 Hz oscillation; the motion is essentially rigid and the two solutions basically overlap. Figure 5(b) refers to a 30 Hz oscillation; the motion quickly becomes nearly chaotic. The wing bends and twists substantially, rolling up almost entirely, as sketched in Fig. 6. When analyzed with slightly different meshes, the 5 Hz case yields

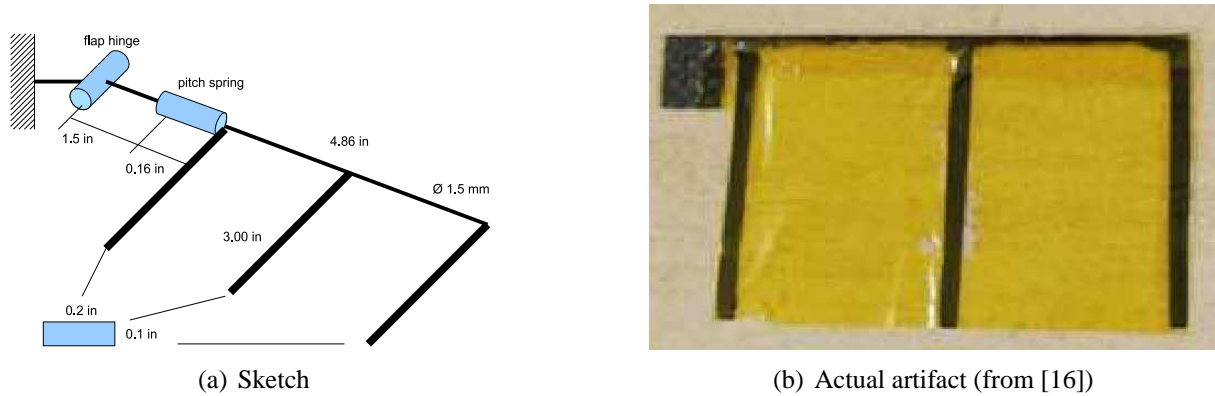


Figure 7: Flexible wing.

substantially identical results, while the 30 Hz case shows an appreciably different behavior. The dependence of the results on the mesh seems to confirm the nearly chaotic nature of the response.

### 3 FLAPPING WING

The development of the proposed shell element within the multibody environment provided by MBDyn is motivated by the need to analyze the fluid-structure coupling problem defined by the very flexible family of wings under development at the University of Maryland within the MAST/CTA program. As a preliminary example, the flapping wing MAV experimentally investigated in [16], illustrated in Fig. 7, is considered.

#### 3.1 Structural Model

The structural model consists of a frame of beam elements connected by a membrane made of shell elements. The length of the spar is 123.44 mm (4.86 in) and the diameter of the circular section is 1.5 mm. The length of the chordwise ribs is 76.20 mm (3 in); their section is rectangular, 2.54 mm (0.1 in) thick and 5.08 mm (0.2 in) wide. The wing root is located at 38.10 mm (1.5 in) spanwise from the flap hinge, where a torsional spring is located. The first chordwise rib is located 4.06 mm (0.16 in) from the wing root. The torsional spring (nonlinear, although its actual characteristic is not currently modeled) allows to passively control the pitch change as a function of the wing motion and inertial and aerodynamic loads.

The structural properties are listed in Table 1; in some cases they represent reasonable guesses, as the actual properties of the artifact could not be measured. The model is currently being correlated with experimental results; the fitting could probably be improved, although it already appears to reproduce relatively well the observed behavior.

Figure 8 illustrates the motion of the wing when performing a half-cycle at zero reference pitch angle, subjected to pure drag external forces (i.e. nodal forces opposite to the absolute velocity of the nodes).

#### 3.2 Aerodynamic Model and Fluid-Structure Interaction

The aerodynamics of flapping wing for MAV are characterized by substantial unsteady low-Mach, low-Reynolds phenomena. Viscosity and unsteadiness play a major role in the description of the dependence of aerodynamic loads on the motion of the structure [6, 15]. For this reason, it is understood that CFD based on unsteady Navier-Stokes equations need to be used.

Table 1: Flapping wing: structural properties.

Carbon-fiber spanwise spar & chordwise ribs		
Density	1600.0	kg/m <sup>3</sup>
Tensile modulus	220.0	GPa
Shear modulus	5.0	GPa
Mylar film		
Density	1390.0	kg/m <sup>3</sup>
Tensile modulus	4.9	GPa
Poisson's modulus	0.3	
Thickness	$2.54 \times 10^{-5}$	mm
Pitch spring		
Stiffness	1.0	N m/radian
Damping	$5.0 \times 10^{-3}$	N m s/radian

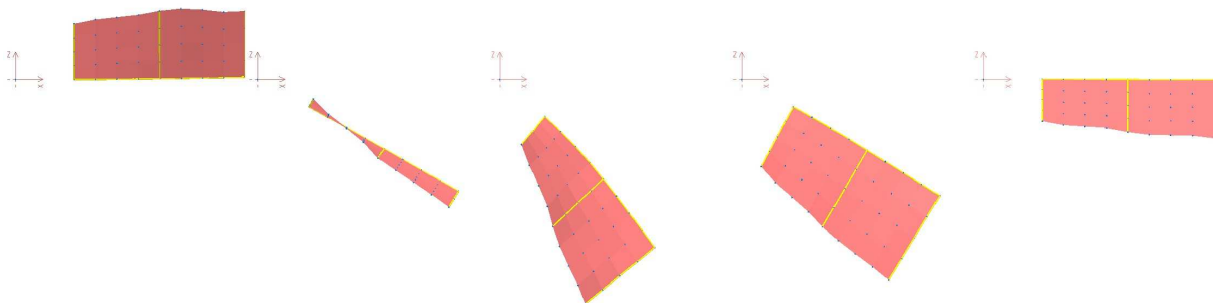


Figure 8: Half-cycle flapping sequence of multibody model of flexible wing.



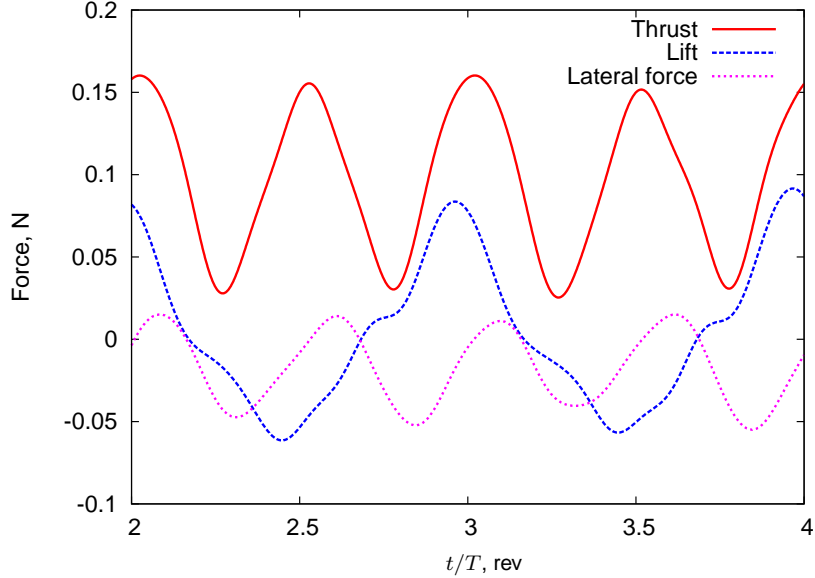


Figure 10: Flapping wing: force components of a single wing in hover.

is probably related to the inaccuracy of the vortex lattice model and to the uncertainties in the structural model. The trend of the thrust with respect to actuation frequency is shown in Fig. 11.

Figure 12 presents the difference of pressure distribution between the upper and lower surfaces on the (deformed) wing at seven points during a complete stroke of the wing,

$$\Delta p = p_u - p_l. \quad (18)$$

The minimal pressure distribution, close to null  $\Delta p$  on the entire wing surface, is obtained at the maximum stroke amplitudes, upward and downward, i.e.  $\beta = 40$  downstroke and  $\beta = -40$  upstroke. These positions correspond to the minimum points of the thrust curve shown in Fig. 10. The maximum thrust is obtained at  $\beta = 0$  always. However, the behaviour of the lift force is different for the two cases. During downstroke, the maximum positive  $\Delta p$  peak is on the leading edge, while during upstroke, close to the leading edge, the maximum negative  $\Delta p$  peak can be observed. The lift distribution curve of Fig. 10 shows that the positive lift obtained close to  $\beta = 0$  downstroke is larger, in absolute value, than the negative value obtained close to  $\beta = 0$  upstroke; this corresponds to the pressure distribution behaviour shown in Fig. 12.

#### 4 CONCLUSIONS AND FUTURE WORK

This work presented the implementation of a 4-node shell element within the free multibody solver MBDyn to support the modeling and the analysis of flapping wing Micro-Aerial Vehicles. In order to provide realistic aerodynamic forces, the structural solver has been coupled to an existing in-house implementation of lifting surface and free wake analysis based on a vortex-lattice approach. An original general-purpose, meshless boundary interfacing approach based on Moving Least Squares with Radial Basis Functions has been used. Extensive validation of the shell implementation has been presented. Encouraging preliminary results have been obtained from the modeling and analysis of the dynamics and aeroelasticity of a very flexible flapping wing model. Future activity will address the coupling of the structural analysis with unsteady Navier-Stokes for high-fidelity fluid-structure coupling, and extensive parametric investigation of the models to improve the understanding of the physics of the problem and

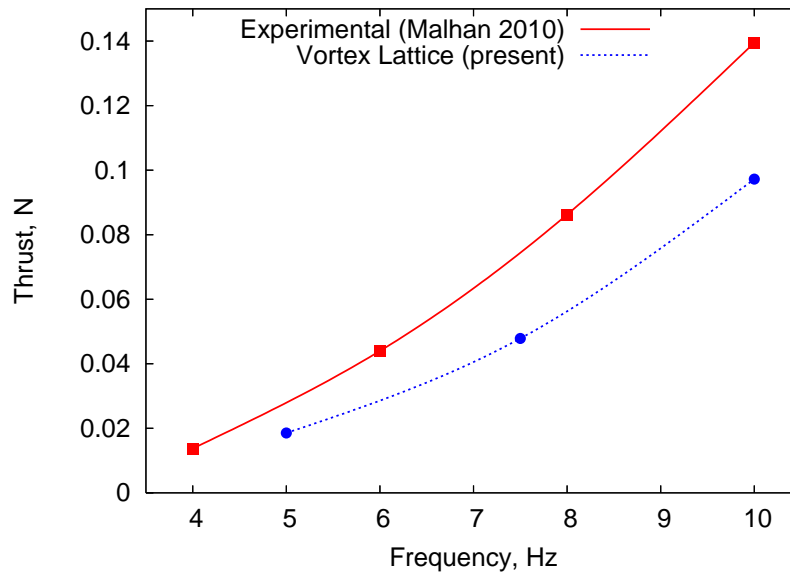


Figure 11: Flapping wing: mean thrust of a single wing as a function of flapping frequency.

support future designs.

## 5 ACKNOWLEDGEMENT

The authors acknowledge Professor Inderjit Chopra for partial support from University of Maryland under Subaward Q334903 in the framework of US Army's MAST CTA Center for Microsystem Mechanics.

## REFERENCES

- [1] Rafal Żbikowski. On aerodynamic modelling of an insect-like flapping wing in hover for micro air vehicles. *Phil. Trans. R. Soc. Lond. A*, 360:273–290, 2002. doi:10.1098/rsta.2001.0930.
- [2] S. A. Ansari, R. Żbikowski, and K. Knowles. Aerodynamic modelling of insect-like flapping flight for micro air vehicles. *Progress in Aerospace Sciences*, 42:129–172, 2006. doi:10.1016/j.paerosci.2006.07.001.
- [3] S. A. Ansari, R. Żbikowski, and K. Knowles. Non-linear unsteady aerodynamic model for insect-like flapping wings in the hover. part 1: methodology and analysis. *J. Aerospace Engineering*, 220:61–83, 2006. doi:10.1243/09544100JAERO49.
- [4] W. Shyy, Y. Lian, J. Tang, H. Liu, P. Trizila, B. Stanford, L. Bernal, C. Cesnik, P. Friedmann, and P. Ifju. Computational aerodynamics of low Reynolds number plunging, pitching and flexible wings for MAV applications. *Acta Mechanica Sinica*, 24(4):351–373, 2008. doi:10.1007/s10409-008-0164-z.
- [5] H. Liu and H. Aono. Size effects on insect hovering aerodynamics: an integrated computational study. *Bioinspiration & Biomimetics*, 4:015002 (13pp), 2009. doi:10.1088/1748-3182/4/1/015002.
- [6] Ria Malhan, Vinod K. Lakshminarayan, James Baeder, and Inderjit Chopra. Investigation of aerodynamics of rigid flapping wings for MAV applications: CFD validation. In *AHS Specialists Conference*, Tempe, AZ, January 25–27 2011.

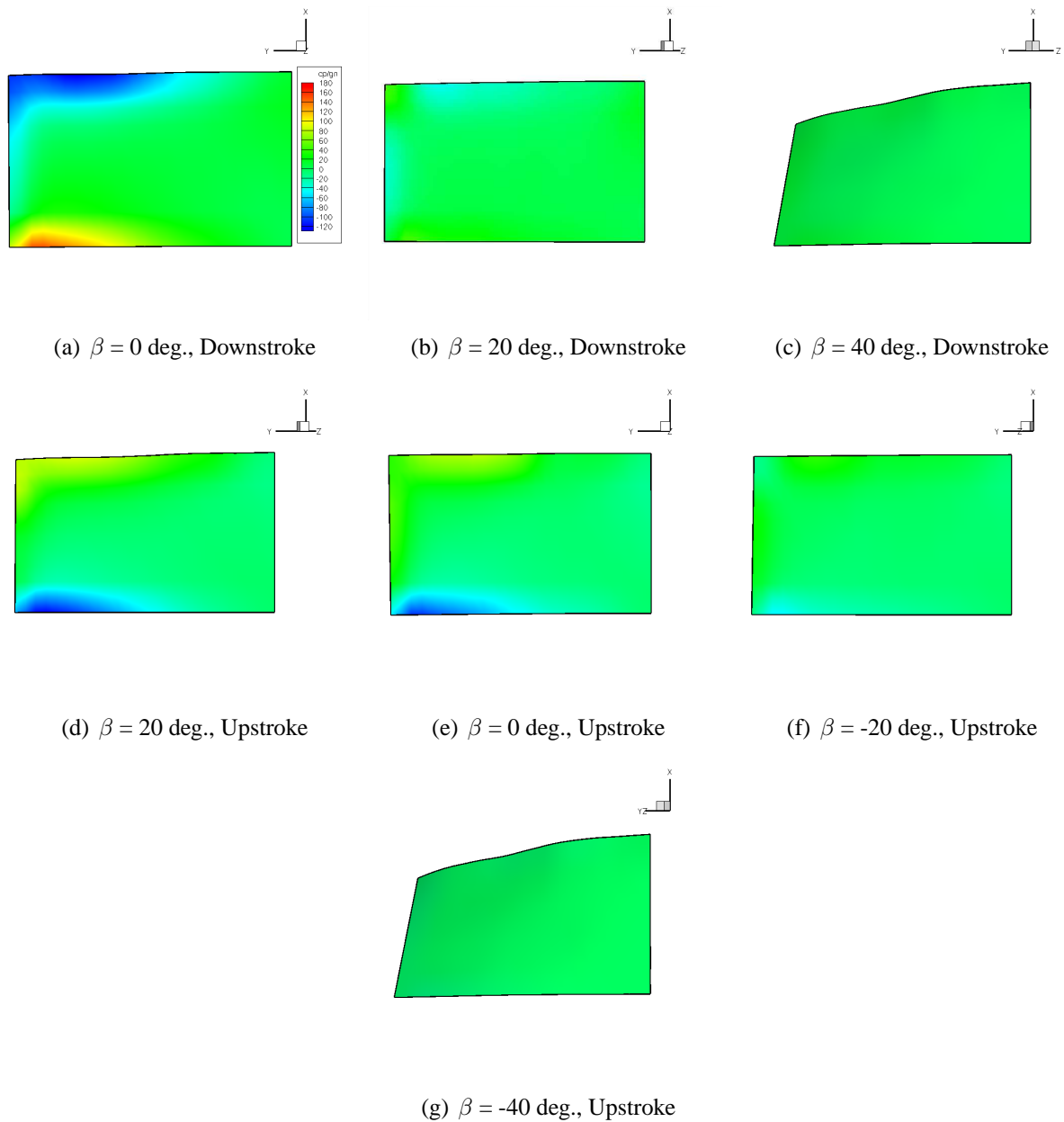


Figure 12: Flapping wing: pressure coefficient during a complete stroke.

- [7] Beerinder Singh. *Dynamics and Aeroelasticity of Hover Capable Flapping Wings: Experiments and Analysis*. PhD thesis, Department of Aerospace Engineering, University of Maryland, 2006.
- [8] Beerinder Singh and Inderjit Chopra. Dynamics of insect-based flapping wings: Loads validation. In *47th SDM Conference*, Newport, Rhode Island, May 1–4 2006. AIAA 2006-1663.
- [9] Bret W. Tobalske and Kenneth P. Dial. Flight kinematics of black-billed magpies and pigeons over a wide range of speeds. *Journal of Experimental Biology*, 199:263–280, 1996.
- [10] Michael H. Dickinson, Fritz-Olaf Lehmann, and Sanjay P. Sane. Wing rotation and the aerodynamic basis of insect flight. *Science*, 284, June 18 1999.
- [11] R. J. Wood, S. Avadhanula, M. Menon, and R. S. Fearing. Microrobotics using composite materials: The micromechanical flying insect thorax. In *2003 IEEE International Conference on Robotics & Automation*, Taipei, Taiwan, September 14–19 2003.
- [12] Rafal Żbikowski, Cezary Galiński, and Christopher B. Pedersen. Four-bar linkage mechanism for insect-like flapping wings in hover: Concept and an outline of its realization. *Journal of Mechanical Design*, 127(4):817–814, July 2005. doi:10.1115/1.1829091.
- [13] W. Shyy, Y. Lian, S. K. Chimakurthi, J. Tang, C. E. S. Cesnik, B. Stanford, and P. G. Ifju. Flexible wings and fluid-structure interactions for micro-air vehicles. In D. Floreano et al., editor, *Flying Insects and Robots*, chapter 11. Springer-Verlag, Berlin Heidelberg, 2009. doi:10.1007/978-3-540-89393-6\_11.
- [14] Hao Liu. Integrated modeling of insect flight: From morphology, kinematics to aerodynamics. *Journal of Computational Physics*, 228(2):439–459, February 2009. doi:10.1016/j.jcp.2008.09.020.
- [15] Weixing Yuan, Richard Lee, Eric Hoogkamp, and Mahmood Khalid. Numerical and experimental simulations of flapping wings. *International Journal of Micro Air Vehicles*, 2(3):181–208, September 2010. doi:10.1260/1756-8293.2.3.181.
- [16] Ria Malhan, Moble Benedict, and Inderjit Chopra. Experimental investigation of a flapping wing concept in hover and forward flight for micro air vehicle applications. In *66th AHS Forum*, Phoenix, Arizona, May 11–13 2010.
- [17] Wei Shyy, Peter Ifju, and Dragos Viieru. Membrane wing-based micro air vehicles. *Applied Mechanics Reviews*, 58(4):283–301, July 2005. doi:10.1115/1.1946067.
- [18] Gian Luca Ghiringhelli, Pierangelo Masarati, and Paolo Mantegazza. A multi-body implementation of finite volume beams. *AIAA Journal*, 38(1):131–138, January 2000. doi:10.2514/2.933.
- [19] D. Chandar and M. Damodaran. Computational study of the free flight of a flapping wing at low reynolds numbers. In *46th AIAA Aerospace Sciences Meeting*, Reno, Nevada, January 7–10 2008. AIAA 2008-420.
- [20] Satish K. Chimakurthi, Bret K. Stanford, Carlos E. S. Cesnik, and Wei Shyy. Flapping wing CFD/CSD aeroelastic formulation based on a corotational shell finite element. In *50th SDM Conference*, Palm Springs, California, May 4–7 2009. AIAA 2009-2412.
- [21] Wojciech Witkowski. 4-node combined shell element with semi-EAS-ANS strain interpolations in 6-parameter shell theories with drilling degrees of freedom. *Computational Mechanics*, 43(2):307–319, 2009. doi:10.1007/s00466-008-0307-x.

- [22] J. Chróscielewski and W. Witkowski. Four-node semi-EAS element in six-field nonlinear theory of shells. *International Journal for Numerical Methods in Engineering*, 68(11):1137–1179, 2006.
- [23] T. Merlini and M. Morandini. The helicoidal modeling in computational finite elasticity. Part II: Multiplicative interpolation. *Int. J. Solids Struct.*, 41:5383–5409, 2004. Erratum on *Int. J. Solids Struct.* 42, p. 1269 (2005).
- [24] Pierangelo Masarati and Gian Luca Ghiringhelli. Characterization of anisotropic, non-homogeneous plates with piezoelectric inclusions. *Computers & Structures*, 83(15-16):1171–1190, June 2005.
- [25] K. Y. Sze, X. H. Liu, and S. H. Lo. Popular benchmark problems for geometric non-linear analysis of shells. *Finite Elements in Analysis and Design*, 40:1551–1569, 2004. doi:10.1016/j.finel.2003.11.001.
- [26] Giuseppe Quaranta, Pierangelo Masarati, and Paolo Mantegazza. Assessing the local stability of periodic motions for large multibody nonlinear systems using POD. *Journal of Sound and Vibration*, 271(3–5):1015–1038, 2004. doi:10.1016/j.jsv.2003.03.004.
- [27] P. Masarati. Direct eigenanalysis of constrained system dynamics. *Proc. IMech. E Part K: J. Multi-body Dynamics*, 223(4):335–342, 2009. doi:10.1243/14644193JMBD211.
- [28] Giuseppe Quaranta, Giampiero Bindolino, Pierangelo Masarati, and Paolo Mantegazza. Toward a computational framework for rotorcraft multi-physics analysis: Adding computational aerodynamics to multibody rotor models. In *30th European Rotorcraft Forum*, pages 18.1–14, Marseille, France, 14–16 September 2004.